A Tricycle Model to Accurately Control an Autonomous Racecar with Locked Differential

Ayoub Raji[1,2,*], Nicola Musiu[1,*], Alessandro Toschi[1], Francesco Prignoli[1], Eugenio Mascaro[1], Pietro Musso[1], Francesco Amerotti[3], Alexander Liniger[4], Silvio Sorrentino[1], Marko Bertogna[1]

Abstract— In this paper, we present a novel formulation to model the effects of a locked differential on the lateral dynamics of an autonomous open-wheel racecar. The model is used in a Model Predictive Controller in which we included a micro-steps discretization approach to accurately linearize the dynamics and produce a prediction suitable for real-time implementation. The stability analysis of the model is presented, as well as a brief description of the overall planning and control scheme which includes an offline trajectory generation pipeline, an online local speed profile planner, and a low-level longitudinal controller. An improvement of the lateral path tracking is demonstrated in preliminary experimental results that have been produced on a Dallara AV-21 during the first Indy Autonomous Challenge event on the Monza F1 racetrack. Final adjustments and tuning have been performed in a high-fidelity simulator demonstrating the effectiveness of the solution when performing close to the tire limits.

Index Terms— Autonomous racing, model predictive control, tricycle model, single-track model, vehicle modeling

Fig. 1. Dallara AV-21 - TII UNIMORE Racing during the Indy Autonomous Challenge at MIMO 2023 in the Monza F1 circuit. ©Autodromo Nazionale Monza

I. INTRODUCTION

The vehicle models used within model-based motion planning and control algorithms for autonomous driving depend on a trade-off between simplicity and accuracy, which is closely tied to the specific application. The most common models in the literature are the point-mass model, kinematic single-track model, dynamic single-track model, double-track model, and multi-body model [1]. In urban scenarios, where motion can be identified through purely geometric approaches, due to the minimal slip angles, it is generally sufficient to use a kinematic single-track model [2][3].

In more complex maneuvers that produce not negligible lateral accelerations, the dynamic single-track model is commonly used. Dynamic effects, such as tire forces, and additional states such as lateral velocity, are considered. In [4][5], the model is used in a feedback-feedforward steering control scheme guaranteeing accuracy and stability. In more recent works, the Model Predictive Control (MPC) using the single-track model has become widely used [6]. Several researchers demonstrated the effectiveness of this approach to control sport road cars close to the limit of handling exploiting more accurate tire models to represent

[1]University of Modena and Reggio Emilia, Italy
{firstname.lastname}@unimore.it,
{291709;304753}@studenti.unimore.it,
[2]University of Parma, Italy
[3]Hipert srl, Italy
francesco.amerotti@hipert.it
[4]Computer Vision Lab, ETH Zurich, Switzerland
alex.liniger@vision.ee.ethz.ch
∗The authors contributed equally.

the lateral forces [7][8][9]. We implemented a similar solution competing as the TII Unimore Racing team to the Indy Autonomous Challenge (IAC[1]), an autonomous racing competition among universities from all around the world. Relying on the modeling of a single-track model exploited in an MPC, we achieved a top speed of 270 km/h and a maximum lateral acceleration of up to 25 m/s² in the first events on oval tracks [10]. To get a better overview of the methods used in the autonomous racing literature we refer to [11].

Despite the overall effectiveness of the bicycle model, its classical formulation has some limitations for an open-wheel racecar, e.g. assuming an open-differential. This leads to neglecting the contribution of longitudinal forces on the yaw moment. Indeed, on a road course like the Monza F1 racetrack, where the latest event of the IAC has been held, this model presents limitations because it is not able to distinguish between tight curves and wide-radius curves. Consequently, it cannot reproduce any dynamic behavior, such as nose-in/nose-out [12], caused by a locked differential. Potentially, the parameters of the constitutive equations can be tuned to enhance optimal accuracy in only one of the two scenarios mentioned above. However, this can lead to highly unbalanced axle characteristics (high rear cornering stiffness), resulting in numerical instability of the model at low speed.

In response to these challenges, the main contributions of this paper are as follows:

- A three-wheel model (tricycle model) has been developed to account for the dependence on the path curvature. By estimating the longitudinal forces at the rear axle and, consequently, the contribution on the yaw moment, we can anticipate a possible nose-out resulting in an improvement of the vehicle modeling and therefore the trajectory tracking. To the best of our knowledge, the model proposed is new in the literature.
- Due to the characteristics of the system at low speed, a kinematic model has been used for low-speed maneuvers. To keep this speed threshold low, a stability analysis of the dynamic model has been performed finding the suitable discretization step time needed to keep the model stable, and implementing a micro-step discretization approach in the MPC to make it suitable for real-time execution.

In Section II we present the tricycle model formulation and its stability analysis. The MPC formulation, including the micro-step model discretization, is described in Section III. Even though they do not present any novel contribution, the high-level planning scheme and the low-level longitudinal controller used in the whole planning and control scheme are briefly reported in Section IV and Section V, respectively. The model validation, preliminary experimental results, and final results of the proposed solution are presented in Section VI. Conclusions and future works are discussed in Section VII.

II. VEHICLE MODELING

The Dallara AV-21, shown in Figure 1, is based on the chassis and suspension of the Indy Lights IL-15. The internal combustion engine is equipped with a turbocharger that increases the engine torque to over 500 Nm. The torque is transmitted to the rear wheels through a rigid axle (no differential is installed). For vehicle handling, this represents a significant limitation, especially on road course tracks where both tight and wide-radius curves can be found. This, combined with a stable setup choice, leads the car to exhibit a nose-out behavior on turn entry, which can become a nose-in behavior on turn exit [12].

A. Accurate Multi-Body Model

In a context where on-track test sessions are often limited and expensive, multi-body models can offer detailed and in-depth simulations, significantly expediting the development process and allowing engineers to virtually test various scenarios and control strategies before transitioning to expensive and risky physical tests.

An accurate vehicle model is of paramount importance in this application. It provides an efficient solution to optimize vehicle performance and to test planning and control algorithms using a reliable ground truth. Therefore, a multi-body model of the Dallara AV-21 has been developed on the modeling tool Dymola [13] using the VeSyMA - Motorsports libraries [14]. The model includes all the longitudinal, lateral, and vertical dynamics of the real system. Compared to the previous version mentioned in [15], particular attention has

been focused on modeling the suspension dampers, the tire's thermal behavior, and the powertrain inertial characteristic. Accurate sub-models for the locked differential, the braking system, and the centrifugal clutch have been included as well.
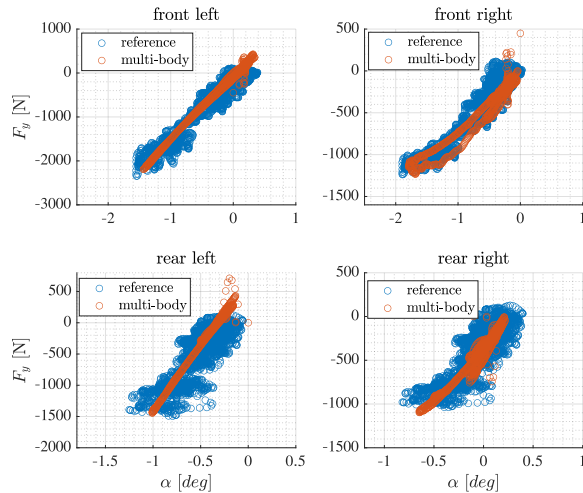
Fig. 2. A comparison between experimental data and the multibody model is presented. The slip angle is plotted on the x-axis, and the estimated wheel force is shown on the y-axis. It can be observed that the inner wheels (right side), where there is less vertical load acting, are working in the non-linear region of the tire.
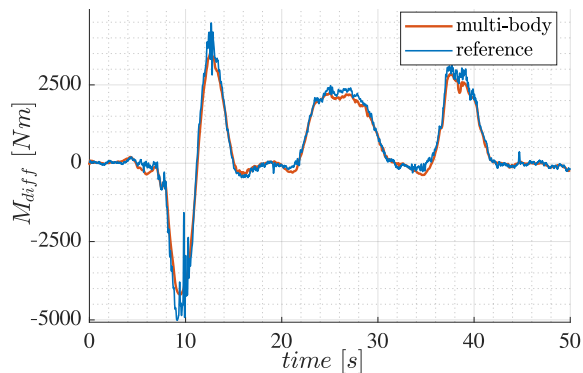
Fig. 3. Comparison between the experimental measurement of the yaw moment due to the locked differential (through slip ratio calculations), used as a reference (in blue), and the estimation from the multi-body model (in orange). The noisy reference is related to the accuracy of the estimation and the highly nonlinear nature of the measurement. The higher the curvature, the greater the resisting yaw moment to turn in. Here, the central section of the Monza track is shown, including Variante 2 and the Lesmo turns.

As can be seen in Figures 2 and 3, the overall accuracy is good enough for the objective, thus the model is used as ground truth for calibrating the simplified model and for testing the control algorithms.

B. Locked Differential Tricycle Model

For what concerns the front axle, the tricycle formulation is derived from the classic single-track model expressed in curvilinear coordinates, while the rear axle is derived from the double-track model. The final structure is shown

in Figure 4. The new state-space model is described by the state vector $\tilde{x} = [s; n; \mu; v_x; v_y; r; \delta; D]$ and the input vector $\tilde{u} = [\Delta\delta; \Delta D]$, where s, n, and μ represent the progress along the path, the orthogonal deviation from the path, and the local heading. The motion equations are expressed as the derivative of the longitudinal v_x and the lateral v_y velocities and the yaw rate r. δ represents the steering angle and D is the desired longitudinal acceleration. $\Delta\delta$ and ΔD represent the derivatives of the inputs. The whole set of equations can be found in [10].
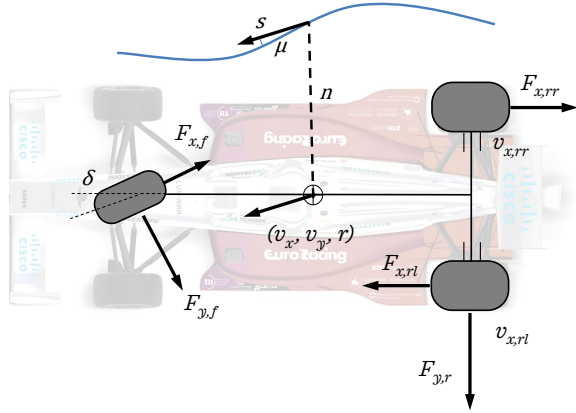
Fig. 4. Scheme of the three-wheels model, in curvilinear coordinates, included in the MPC.

In the motion equations, we included the longitudinal forces required for traction and braking F_{xf}^{cmd} and F_{xr}^{cmd}, and the contribution of the longitudinal forces on the total yaw moment, M_{diff}. The set of equations is presented here:

$$\dot{v}_x = \frac{1}{m}\left(F_{xr}^{cmd} - F_d - F_{yf}\sin(\delta) + F_{xf}^{cmd}\cos(\delta) + mv_y r\right),$$
(1a)

$$\dot{v}_y = \frac{1}{m}\left(F_{yr} + F_{yf}\cos(\delta) + F_{xf}^{cmd}\sin(\delta) - mv_x r\right),$$
(1b)

$$\dot{r} = \frac{1}{I_z}\left(M_{diff} + l_f\left(F_{yf}\cos(\delta) + F_{xf}^{cmd}\sin(\delta)\right) - l_r F_{yr}\right),$$
(1c)

where m and I_z are the mass and the inertia of the vehicle, and l_f and l_r are the front and rear wheelbase. F_{yf} and F_{yr} are the lateral forces generated in the interface between the road and the tires, and F_d is the aerodynamic drag. The rolling resistance is included in the longitudinal equilibrium as well. From now on, the index i^{th} is used to identify the axle (front, rear), while the index j^{th} identifies the vehicle side (left, right).

The yaw moment is derived from the rotational equilibrium of the rear axle in the Z-axis direction:

$$M_{diff} = \frac{1}{2}(F_{x,rr} - F_{x,rl}) \cdot t_r.$$
(2)

where t_r represents the rear axle track. The longitudinal forces include both the contribution of the locked differential and the traction dynamics: $F_{x,rj} = F'_{x,rj} + F_{x,rj}^{cmd}$. The longitudinal forces experienced during vehicle coasting are estimated using the non-linear Pacejka tire model:

$$F'_{x,rj} = D_{x,rj}\sin\left(C_{x,r}\tan^{-1}(B_{x,r}\,k_{x,rj})\right)$$
(3)

$D_{x,rj} = \mu_r F_{z,rj}$, B_r and C_r are the macro-parameters of the magic formula [18] and $F_{z,rj}$ represents the vertical load on the jth wheel, as will be shown in 6. The slip ratio is expressed as

$$k_{x,rj} = \frac{v_x - v_{x,rj}}{v_x}$$
(4)

and depends on the ideal speed of the rear wheels, taking into account the vehicle's geometry and the track's layout:

$$v_{x,rj} = r \cdot \left(R \pm \frac{t_r}{2}\right).$$
(5)

In the equation 5, R is the turning radius. To account for the traction forces, we have included a straightforward formulation based on the commanded acceleration. We defined $F_{x,r}^{cmd} = f(D)$, which is distributed between the rear wheels through the lateral load transfer. In this way, we can check for a possible nose-in during the phase of turn-exit.

Considering the tricycle structure, it proved necessary to include a model for estimating the lateral load transfer and, consequently, to distribute the vertical load on each wheel. Hence, the standard model based on the roll axis [19] has been included. This has been employed exclusively for the rear axle, as the axle effective characteristic is used for the front one. The vertical load on each wheel is computed:

$$F_{z,rj} = \frac{1}{2}F_{z,r} \pm \Delta F_{z,r}^{lat}$$
(6)

where the global load on the rear axle $F_{z,r}$ is the sum of the static load $F_{z,r}^0$, the aerodynamic effect $F_{z,r}^{aero}$ [10] and the longitudinal load transfer $\Delta F_{z,r}^{long}$ contributions [19]. The lateral load transfer is estimated with the relation:

$$\Delta F_{z,r}^{lat} = F_{y,r}\frac{h_r}{t_r} + \frac{M_y}{t_r}\frac{K_r}{K_{tot}},$$
(7)

where h_r is the height of the roll axis at the rear axle, K_r and K_{tot} are the rear axle roll stiffness and the total roll stiffness. $M_y = m \cdot a_y \cdot q$ and $F_{y,r}$ represent the moment and force generated by the inertia on the roll axis. To estimate the latter, a rotational equilibrium of the whole vehicle on the Z-axis is performed, from which it follows that:

$$F_{y,r} = (m \cdot a_y \cdot l_f + M_{diff}^0) \cdot \frac{1}{l}$$
(8)

Here, l and q represent, respectively, the wheelbase and the Z-distance between the center of gravity and the roll axis. M_{diff}^0 represents the yawing moment calculated by the model in the previous integration step and a_y is calculated starting from the motion field.

The employment of this simplified roll-axis model for the load transfer estimation is an acceptable approximation since the roll motion of an open-wheel vehicle is negligible. This module allows the model to improve the accuracy in the calculation of the longitudinal forces, and consequently the prediction of the vehicle's pose.

The longitudinal forces are also used to account for the combined slip on the tires. The formulation is based on a friction ellipse, through which a weight factor $G_{y,ri}$ is computed as in [10]. Likewise, the weight factor is defined for the front axle.

C. Model Stability Analysis

Representing a racecar with a mathematical model always requires special care. This is because the parameters of the model, especially those concerning the tires, can make the differential equation system very stiff and subject it to numerical instability if the integration method (or the step size) is not carefully chosen. The original setup proposed for oval tracks uses the numerical method Runge-Kutta 4 (RK4) and a time-step $h = 0.04s$ [10], which guarantees the stability only for longitudinal speed greater than $28\ m/s$ on the single-track, and $32\ m/s$ on the three-wheels model. This is not suitable for a road course track like Monza, where the speed can reach a minimum of $12\ m/s$ (i.e. Variante 1). To guarantee the numerical stability of the dynamic model at low speeds, it has been chosen an integration step size small enough to include the poles of the linearized system within the stability region defined by the numerical method [16].

The overall results of the stability analysis for the tricycle model are shown in Figure 5. An optimal value of time-step $h = 0.008s$ was chosen to cover all significant speed ranges expected on the track, i.e. $v_x^{min} = 8m/s$. Below this threshold, the kinematic model written in the dynamic model states is used to avoid numeric oscillations on the solution. The two models are blended similarly to how it has been presented in [17].

In the first steps of the development and the experimental testing, the chosen integration method has been the explicit Euler, which provides better computation times compared to higher-order methods (i.e. RK4). As described in Section VI, this choice has been changed in the final tests.
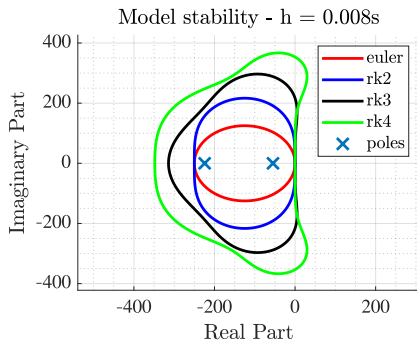
Fig. 5. Poles for the three-wheels model at $v_x = 8m/s$. The proposed step size for the integration allows the system poles to lay within the stability region of the explicit Euler method.

III. MPC PROBLEM FORMULATION

The model in curvilinear coordinates described in Section II-B is used in an extension of the MPC presented in [10]. The main differences from the previous work are:

- A velocity tracking weight q_v instead of a slack variable to follow more strictly the velocity reference.
- A weight on the yaw rate q_r which aims to mitigate potential oscillations caused by bumpy portions of the track or disturbances in the steering actuation.

- Additional independent variables, and an improvement of the model discretization.
- The inputs are the derivative of the steering angle and the requested longitudinal acceleration instead of using the throttle and brake commands.

The cost function is formulated as:

$$J_{MPC}(x_t, u_t) = q_n n_t^2 + q_\mu \mu_t^2 + q_v v_t^2 + q_r + u^T R u + B(x_t) \quad (9)$$

where q_n and q_μ are path following weights. The regularization term $B(x_k) = q_B \alpha_r^2$ penalizes the rear slip angle, while $u^T R u$ is a regularizer on the input rates where R is a diagonal weight matrix.

The MPC problem is formulated as

$$\min_{X,U} \quad \sum_{t=0}^{T} J_{MPC}(x_t, u_t) \quad (10a)$$

$$s.t. \quad x_0 = \hat{x}, \quad (10b)$$

$$x_{t+1} = f_t^d(x_t, u_t), \quad (10c)$$

$$x_t \in X_{track} \quad x_t \in X_{ellipse}, \quad (10d)$$

$$a_t \in \boldsymbol{A}, u_t \in \boldsymbol{U}, t = 0, \dots, T. \quad (10e)$$

where $X = [x_0, ..., x_T]$, and $U = [u_0, ..., u_T]$. $X_{ellipse}$ represents a friction ellipse constraints, and X_{track} constrains the lateral deviation n ensuring that the vehicle stays on the track. $\hat{x}$ is the current curvilinear state and T is the prediction horizon. $\boldsymbol{A}$ and $\boldsymbol{U}$ are box constraints for the physical inputs $a = [\delta; D]$ and their rate of change u.

A. Locked Differential Model Progression

In the definition of the optimization problem, the critical issue is advancing the prediction without the ability to track the evolution of M_{diff} with respect to the previous iteration. which is essential for estimating the correct value of the load transfer and the yaw moment itself. One solution could be the introduction of an additional variable to the state vector but this would increase the dimension of the optimization problem raising the computational time. Therefore, the M_{diff}^0, which is the initial yaw moment for each step time t in the control horizon, is calculated (with the same formulation as in Section II) before the execution of the control optimization, using the states from the latest MPC prediction horizon, and included as an independent variable. This is an acceptable simplification considering that having a stable model, a well-posed optimization problem, and a high-frequency running control scheme, the prediction of the MPC should not produce any abrupt change compared to the previous one.

B. Micro-steps Model Discretization

The MPC is executed in real-time at a frequency of 100Hz and a time horizon of 2.6s with a sampling time of Δt = 40ms. In the previous version [10], the model was discretized in time $f_t^d(x_t, u_t)$ with the same sampling time of the optimization:

$$x_{k+1} = \Phi_k(x_k, \ u_k, \Delta t), \quad (11)$$

where Φ_k is the chosen integrator (Euler or RK4). However, this does not adhere to the outcome of the stability analysis

presented in Section II-C. Therefore, a micro-step discretization approach has been applied

$$\Phi_k(x_k, \ u_k, \Delta t) = \underbrace{\Phi_k(\ldots \Phi_k(x_k, u_k, h), u_k, h))}_{\Delta t/h \text{ times}} \quad (12)$$

where h indicates a chosen sampling time divisor of Δt, in our case h = 8ms. This can also be seen as performing Φ_k with $\Delta t/h$ step sizes of h and picking the resulting x_{k+i} at each Δt.

IV. PLANNING

A. Global Trajectory

To generate an optimal race line we used the global planner presented in [10]. Despite its effectiveness in producing an optimal path, the generation of different speed profiles is not trivial and rapid. For this reason, a tool has been designed to compute and optimize the velocity profile for the generated path. Its primary objective is to find the most efficient velocity profile that minimizes lap time while respecting the specified constraints.

The first constraint pertains to the lateral acceleration,

$$v_x^2 \cdot \rho < a_y^{max}(v_x), \quad (13)$$

where v_x represents the vehicle speed along the path, ρ is the curvature at a particular point, and a_y^{max} is a function that defines the maximum allowable lateral acceleration for a given speed. The values for the maximum lateral acceleration are obtained from a ramp-steer maneuver simulated in the multi-body model presented in II-A.

The second and third constraints focus on the negative and positive longitudinal acceleration.

$$a_{x+}^{max}(v_x) > \frac{\Delta v_x^2}{2\Delta s} > a_{x-}^{max}(v_x) \quad (14)$$

The constraints are determined by the rate of change of the velocity Δv_x^2 divided by twice the rate of change of distance Δs. The equation 14 states that this value must be greater than a_{x-}^{max} and lower than a_{x+}^{max}, which are respectively the maximum permissible deceleration and acceleration for a given speed. The evaluation of the negative acceleration limit is performed by exploiting the braking diagram of the vehicle, accounting for brake balance set-up, longitudinal load transfer, and aerodynamic effects. While the longitudinal limit is found by considering both the limitation in the powertrain and the tire grip.

B. Longitudinal Planner

The Longitudinal Planner dynamically computes speed, acceleration, and jerk profiles based on the real-time status of the vehicle. This module is based on a Linear Model Predictive Control (LMPC) framework, following the standard formulation:

$$\min_{X,U} J = \|x_T - x_{r,T}\|_P^2 + \sum_{t=0}^{T-1} \left(\|x_t - x_{r,t}\|_Q^2 + \|u_t\|_R^2 \right) \quad (15a)$$

$$\text{s.t.} \quad x_{t+1} = Ax_t + Bu_t \quad (15b)$$

$$x_0 = \hat{x} \quad (15c)$$

$$u_t \in \mathcal{U}_t, \quad t = 0, 1, \ldots, T-1 \quad (15d)$$

$$x_t \in \mathcal{X}_t, \quad t = 0, 1, \ldots, T \quad (15e)$$

where $X = [x_0, \ldots, x_T]$, $U = [u_0, \ldots, u_{T-1}]$ and T is the prediction horizon length; P and Q are the terminal and stage cost weighting matrices on the deviation of the state x from the reference x_r; R is the control input cost weighting matrix; $\hat{x}$ is the current state; $\mathcal{X}_t$ and $\mathcal{U}_t$ are constraints on the state and input at time step t. The prediction model is a double integrator including the longitudinal speed v_x and acceleration a_x in the state and the jerk j_x as control input:

$$x = \begin{bmatrix} v_x & a_x \end{bmatrix}^\top, u = j_x \quad (16)$$

$$A = \begin{bmatrix} 1 & T_s \\ 0 & 1 \end{bmatrix}, B = \begin{bmatrix} T_s^2/2 \\ T_s \end{bmatrix} \quad (17)$$

where T_s denotes the sample time. Therefore, the goal is to plan feasible speed and acceleration profiles while minimizing the offline speed profile tracking error. Here, most of the design effort lies on the state and input constraints definition, i.e. $\mathcal{X}_t$ and $\mathcal{U}_t$ respectively. Leveraging the preview of path curvature $\hat{\rho}_t$ and speed $\hat{v}_{x,t}$ over the upcoming prediction horizon, an estimate for lateral acceleration can be derived as $\hat{a}_{y,t} = \hat{\rho}_t \hat{v}_{x,t}^2$. This estimate is then used to compute the bounds over the prediction horizon on the longitudinal acceleration, according to the friction ellipse:

$$a_{x,t}^\star = \bar{a}_x^\star(\hat{v}_{x,t}) \sqrt{1 - \left(\frac{\hat{a}_{y,t}}{\bar{a}_y^{max}(\hat{v}_{x,t})} \right)^2}, \quad \star \in \{max, min\} \quad (18)$$

where $\bar{a}_x^{max}(v_x)$, $\bar{a}_x^{min}(v_x)$ and $\bar{a}_y^{max}(v_x)$ are the bounds on the longitudinal and lateral acceleration considering the vertical load only. Eventually, given a desired maximum value of the lateral acceleration $a_y^{max} < \bar{a}_y^{max}(v_x)$, possibly time-varying $a_{y,t}^{max}$, we compute a bound on the longitudinal speed $v_{x,t}^{max}$, depending on the path curvature $\hat{\rho}_t$ as well. The advantage of employing an online longitudinal planner lies in its capacity to guarantee that, whenever the vehicle significantly deviates from the predefined offline speed profile, the controller is provided with speed and acceleration profiles that are feasible concerning the vehicle's dynamics, thereby enhancing safety. Furthermore, this approach opens up the opportunity for online adjustment of the vehicle's longitudinal performance.

V. LOW-LEVEL LONGITUDINAL CONTROL

The MPC, presented in Section III, produces longitudinal velocity v_x^{mpc} and acceleration a_x^{mpc}, which are then converted into throttle and brake signals using a combination of two PI controllers and feed-forward controllers.

To calculate the throttle feed-forward action, the current engine speed, rpm, and the torque target, T_{ref}, are used to query a heuristically constructed look-up table. The torque is determined by the target longitudinal force F_x^{ref}, the radius of the rear wheel r_w, the gear ratio τ_i (with i being the current gear), and the final drive τ_d. The transmission efficiency η_t is included as well:

$$T_{ref} = \frac{F_x^{ref} \cdot r_w \cdot \tau_i \cdot \tau_d}{\eta_t} \quad (19)$$

The force F_x^{ref} indirectly incorporates the target velocity v_x^{mpc} through its dependence on F_d and F_{roll}. It also

directly considers the acceleration target a_x^{mpc} according to the relationship:

$$F_x^{ref} = m \cdot a_x^{mpc} - F_d - F_{roll} + \frac{J_0 \cdot a_x^{mpc}}{r_w^2}, \qquad (20)$$

where J_0 represents the rotational inertia of the mechanics and F_{roll} is defined as in [10]. To ensure that the target does not exceed the tire's longitudinal limit, the actual target used for throttle calculation is the minimum value between F_x^{ref} and $F_{x,r}^{limit}$. The latter is determined using Pacejka's peak factor $D_{x,r}$, already mentioned in Section II-B. However, when the force in 20 is negative, it is converted into a brake signal using the equation 21. Since braking dynamics are significantly simpler than powertrain dynamics, a linear equation can be employed with negligible error:

$$B = \frac{F_x^{tar}}{C_{b,f} + C_{b,f}} \cdot B^{max} \qquad (21)$$

$C_{b,f}$ and $C_{b,r}$ are the brake coefficients determined by the geometry and the characteristic of the braking system, e.g. the disk dimension, and parameterized on the maximum pressure that can be applied in the system, B^{max}. Likewise in the throttle calculation, the actual longitudinal force used in 21 is the minimum between F_x^{ref} and a new threshold $F_{x,b}^{limit}$. Unlike the traction force, braking dynamics involve both the front and rear axles, thus requiring the assessment of the maximum force on both axles. Indeed, the braking limit is proportional to the sum of both $D_{x,f}$ and $D_{x,r}$.

Any errors in the feed-forward actions due to discrepancies in force estimation and other modeling errors were compensated for by the PI controllers, whose actions were added to the feed-forward ones.

VI. RESULTS

A. Model Validation

A comparison between the single-track model and the tricycle model in open-loop is presented in Figure 6. The multi-body model serves as a reference. A time horizon of $2.6s$ (as the MPC horizon) is set to highlight position and yaw error over the entire time horizon. It is evident that the prediction of the single-track model in tight-radius curves estimates a larger effective curvature radius, whereas in wide-radius curves the prediction would be the opposite. Concerning the single-track, this result is achieved through a proper tuning of the parameters of the constitutive equations, which represents a trade-off among all the curves of the Monza racetrack. As preliminary introduced in Section I, improving the model to perfectly fit tight-radius curves will decrease performance in wide-radius turns, and vice versa. The tricycle model enhanced by the contribution of the locked differential, using a single axle characteristic calibration, guarantees a better estimation over the entire track.
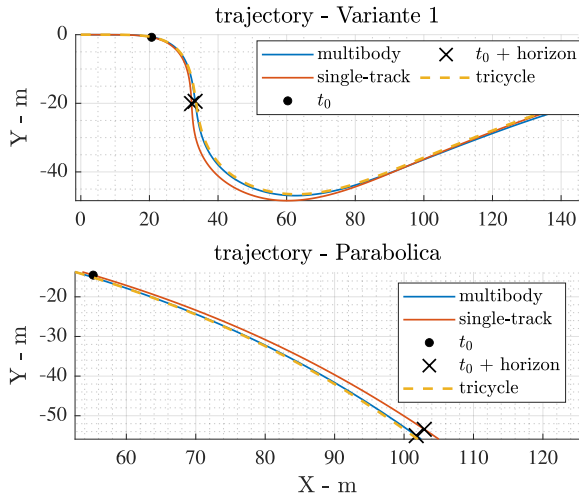
The results of the open loop scenarios are summarized in Table I, where e_y and e_ψ indicate the lateral (m) and heading (°) error respectively. The Lesmo turns are not included in the table as they did not produce significant data.

TABLE I
LATERAL ERROR e_y AND HEADING ERROR e_ψ

	Variante 1		Variante 2		Ascari		Parabolica	
	st	$tric$	st	$tric$	st	$tric$	st	$tric$
e_y	1.22	0.23	1.68	0.80	2.26	0.17	1.97	0.38
e_ψ	4.14	0.86	4.98	2.19	3.98	0.18	1.87	0.41

B. Preliminary Experimental Results

The on-track experimental results of the controller using the tricycle model, compared to the single-track model, are presented. Similarly to [15], an Extended Kalman Filter (EKF) is used to filter all the signals of the vehicle and produce the states needed by the controller.

The single-track model is defined by the kinematic model in the narrow-radius curves and by the dynamic model in the

Fig. 6.   Monza circuit trajectory: the first one displays Variant 1, the tightest curve on the track, while the second one showcases Parabolica, one of the curves with the widest radius.
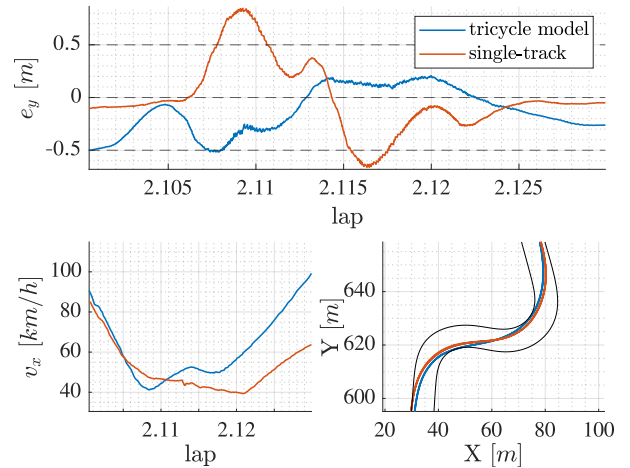
Fig. 7.   Comparison of the two models in the F1 circuit of Monza, Variante 1. See https://youtu.be/jNc9D9T8inw?si=X4n-57CwFl1DXTEE for the on-board video of the best lap.

wide-radius curves as satisfactory and safe tuning could not be found for all the turns of the circuit under consideration.
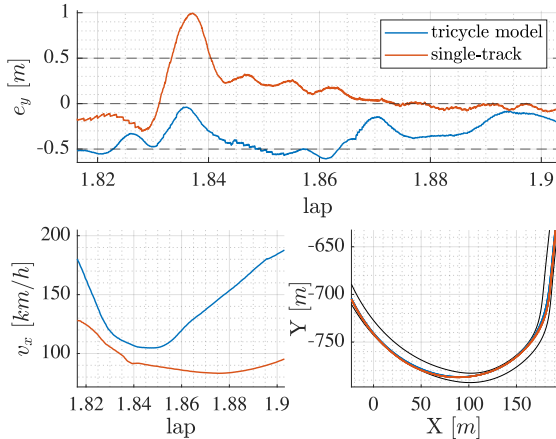
Fig. 8. Comparison of the two models in the F1 circuit of Monza, Parabolica turn.

Figure 7 shows the lateral tracking error and longitudinal velocity with the two models. As expected, compared to the kinematic single-track model, the error using the tricycle model is significantly lower. Similar results are presented in Figure 8, where the Parabolica turn is shown. With the dynamic single-track model, the error increased beyond 1 m, forcing the car to slow down within safe limits. On the contrary, the tricycle model guaranteed a more consistent and stable behavior. As can be noticed in Figure 7 and Figure 8, both the models start the turn maneuvers with a not negligible lateral error. This has been caused mainly by the deterioration of the steering actuator performance at angles close to zero and the setup alignment of the front tires. Another limitation has been the usage of the Euler integrator. The decision was initially taken considering mainly the computational burden. However, this caused an inaccurate discretization when the tire utilization moved towards the non-linear region.
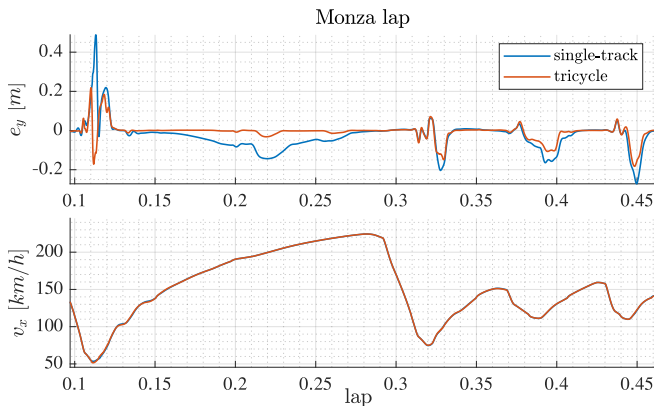
C. Final Results

Despite the interesting insights of Section VI-B, due to the described limitations and the different levels of accuracy in their tuning, we do not consider those results satisfactory enough for a correct comparison of the two models at their best. For this reason, and to demonstrate the performance of the proposed solution close to the very limit of the tire, we present the results in the Dymola multi-body model simulator. These have been produced using the RK4 integrator and after a further improvement of the models' fitting and minor changes on the cost tuning.

In Figures 9 and 10, a comparison between the MPC using the two different models is shown. Optimal tuning of effective axle characteristics has been defined for the single-track model to allow an acceptable error throughout the entire track. Furthermore, it should be noticed that differently from the results of the open-loop validation presented in Section VI-A, due to the closed-loop feedback control the mismatch between the two models is reduced. The different behavior of the single-track model is still evident between slow and fast turns. On the contrary, the tricycle model is capable of making sufficiently accurate predictions over the entire lap and ensuring good consistency in the controller behavior.

In Figure 11, it is visible how the controller is able to exploit the non-linear region of the tire usage, demonstrating its effectiveness close to the vehicle handling limit. A colorbar has been included on the rear tires to highlight the effect of the longitudinal forces on the lateral characteristic. Here, positive combined slip values are associated with traction forces, whereas negative values correspond to braking forces.

VII. CONCLUSIONS

A novel simplified vehicle model, defined as the tricycle or three-wheel model, and its integration into an MPC have been presented. Supported by an offline trajectory generation tool, a longitudinal planer, and a low-level longitudinal controller, the MPC with the proposed model demonstrated a reduction of the lateral error and a more consistent behavior compared to the classical single-track model in experimental

Fig. 9. Comparison of the two models in a simulation on the 1st sector of Monza F1 virtual circuit, driven by the Model Predictive Control (MPC)
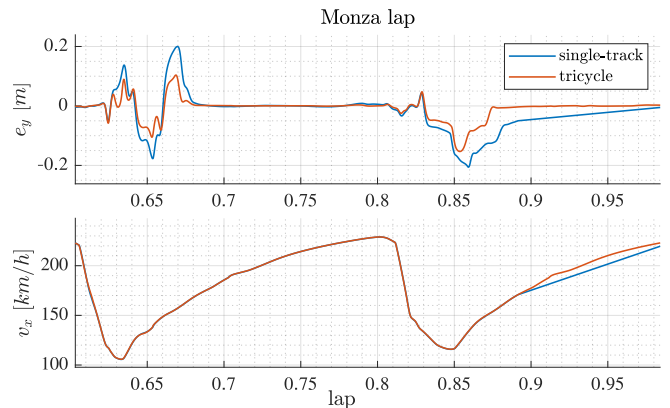
Fig. 10. Comparison of the two models in a simulation on the 2nd sector of Monza F1 virtual circuit, driven by the Model Predictive Control (MPC)
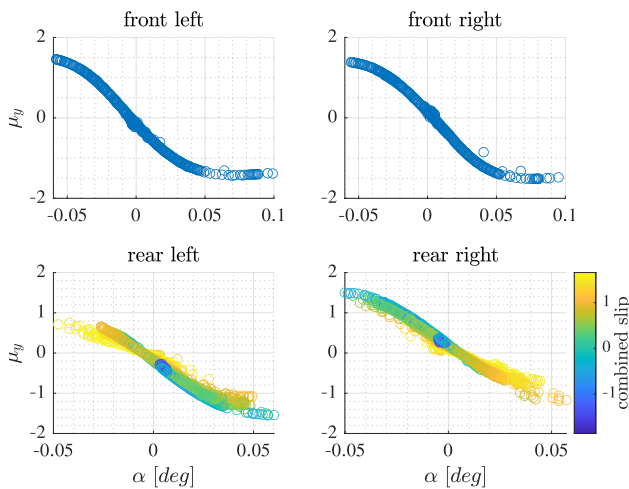
Fig. 11. The characteristic curves of the tires exported from the telemetry of the multi-body model are displayed. It is interesting to note that the controller, with all its modules, can manage the exit phase of the curves at the traction limit.

tests on the Monza F1 racetrack. Further improvements in the model integration showed the capability of the controller to run the vehicle close to its limits on a high-fidelity simulator.

Lastly, it is evident that greater model accuracy can enhance the controller's prediction, improving both stability and performance. However, from the final results, it is clear that a simpler modeling approach, if well formulated, can still suffice for the purpose. This confirms that, depending on the objective and application, model selection has to be a trade-off. For an edge case application, the ideal raceline could be close to the edge of the track. In this scenario, it is important to reduce as much as possible the path tracking error to avoid touching the gravel or the track barriers which could lead to a crash or severe instability.

In future works, this model will be evaluated and extended to adapt to other vehicle configurations like the one with a limited-slip differential.

ACKNOWLEDGMENT

REFERENCES

[1] M. Althoff, M. Koschi and S. Manzinger, "CommonRoad: Composable benchmarks for motion planning on roads," 2017 IEEE Intelligent Vehicles Symposium (IV), Los Angeles, CA, USA, 2017, pp. 719-726.

[2] J. Kong, M. Pfeiffer, G. Schildbach and F. Borrelli, "Kinematic and dynamic vehicle models for autonomous driving control design," 2015 IEEE Intelligent Vehicles Symposium (IV), Seoul, Korea (South), 2015, pp. 1094-1099.

[3] B. Paden, M. Čáp, S. Z. Yong, D. Yershov and E. Frazzoli, "A Survey of Motion Planning and Control Techniques for Self-Driving Urban Vehicles," in IEEE Transactions on Intelligent Vehicles, vol. 1, no. 1, pp. 33-55, March 2016

[4] K.L.R. Talvala, K. Kritayakirana, J. C. Gerdes, "Pushing the limits: From lanekeeping to autonomous racing", Annual Reviews in Control, Volume 35, Issue 1, 2011, Pages 137-148.

[5] N. R. Kapania and J. C. Gerdes, "Design of a feedback-feedforward steering controller for accurate path tracking and stability at the limits of handling", Vehicle System Dynamics, 53:12, 2015, 1687-1704

[6] P. Stano, U. Montanaro, D. Tavernini, M. Tufo, G. Fiengo, L. Novella, A. Sorniotti, "Model predictive path tracking control for automated road vehicles: A review", Annual Reviews in Control, Volume 55, 2023.

[7] V. Zhang, S. M. Thornton, and J. C. Gerdes, "Tyre Modeling to Enable Model Predictive Control of Automated Vehicles From Standstill to the Limits of Handling", 14th International Symposium on Advanced Vehicle Control (AVEC 2018).

[8] J. Dallas, M. Thompson, J. Y. M. Goh, and A. Balachandran. "A hierarchical adaptive nonlinear model predictive control approach for maximizing tire force usage in autonomous vehicles." 2023, Field Robotics, 3, 222–242.

[9] J. Talbot, M. Brown, and J. C. Gerdes, "Shared Control up to the Limits of Vehicle Handling," 2023, IEEE Transactions on Intelligent Vehicles.

[10] A. Raji et al., "Motion Planning and Control for Multi Vehicle Autonomous Racing at High Speeds," 2022 IEEE 25th International Conference on Intelligent Transportation Systems (ITSC), Macau, China, 2022, pp. 2775-2782.

[11] J. Betz et al., "Autonomous Vehicles on the Edge: A Survey on Autonomous Vehicle Racing," in IEEE Open Journal of Intelligent Transportation Systems, vol. 3, pp. 458-488, 2022.

[12] W. Bergman, "The Basic Nature of Vehicle Understeer-Oversteer." SAE Transactions, vol. 74, 1966, pp. 387–422. JSTOR

[13] M. Dempsey, "Dymola for Multi-Engineering Modelling and Simulation," IEEE Veh. Power Propuls. Conf. VPPC, pp. 1-6, 2006.

[14] M. Dempsey, G. Fish, J. G. D. Beltran, "High Fidelity Multibody Vehicle Dynamics Models for Driver-in-the-Loop Simulators", Proceedings of the 11th International Modelica Conference, 2015.

[15] A. Raji et al., "er.autopilot 1.0: The Full Autonomous Stack for Oval Racing at High Speeds", arXiv, 2023

[16] G. Fish, "Stability of explicit Euler solvers", https://www.claytex.com/tech-blog/, 2020.

[17] J. Kabzan et al. "AMZ Driverless: The full autonomous racing system." Journal of Field Robotics 37 (2019): 1267 - 1294.

[18] H. B. Pacejka, "Tyre and Vehicle Dynamics", Butterworth-Heinemann, 2002.

[19] A. Guiggiani, "The Science of Vehicle Dynamics: Handling, Braking, and Ride of Road and Race Cars", Springer, 2004.